

# On Pulse Phase Estimation and Tracking of Variable Celestial X-Ray Sources

A. Robert Golshan, *Johns Hopkins University Applied Physics Laboratory*  
Suneel I. Sheikh, *ASTER Labs, Inc.*

## BIOGRAPHY

**Robert Golshan** is a senior professional staff at the Johns Hopkins University Applied Physics Laboratory. Robert has more than ten years of experience in analysis, simulation, and design of satellite communication and navigation systems. He received his B.S. and M.S. degrees from the University of Virginia and holds a Ph.D. degree from the University of Southern California all in Electrical Engineering.

**Suneel Sheikh** is Chief Research Scientist at ASTER Labs, Inc., where he is researching various aspects of pulsar-based navigation of space vehicles. He earned his Ph.D. degree from the University of Maryland, where his doctoral dissertation research investigated the use of X-ray pulsars for spacecraft navigation. Prior to this, Suneel has over ten years of industry experience in INS and GPS integration research. He earned his M.S. at Stanford University in Aeronautics and Astronautics, and a Bachelor of Aerospace Engineering and Mechanics and a Bachelor of Mathematics from the University of Minnesota.

## ABSTRACT

In this paper, the arrival times of X-ray photons from variable celestial sources, measured by an X-ray detector onboard a spacecraft, are modeled as a non-homogeneous Poisson random process with a periodic or quasi-periodic rate function. The problem of pulse phase estimation is addressed for the case in which the observed signal frequency is assumed to be constant and known over the observation interval. A maximum-likelihood phase estimator (MLE) is derived, and its performance is analyzed in a Monte-Carlo simulation. The Cramer-Rao theoretical performance bound is also derived and evaluated for this parameter estimation problem and then compared against the MLE results. Next, the problem of pulse phase estimation is considered for the case in which dynamical motion of the spacecraft causes the observed signal frequency to vary considerably over the observation interval. The constant frequency assumption is not valid in this case, and the

observed signal exhibits doppler shifts that may cause the pulse arrival times (or phase epochs) at the detector to drift gradually and in an unpredictable manner over the observation interval. For this scenario, a pulse phase tracking algorithm is proposed that consists of an MLE followed by a digital phase-locked loop (DPLL). Photon arrival times are processed through the proposed algorithm, and the DPLL tracked phase and frequency are plotted to demonstrate its dynamical tracking capability.

## INTRODUCTION

While a vast majority of celestial sources throughout the known universe produce steady, or persistent, amounts of radiation, there are also those whose radiation varies in intensity over time. These variable celestial sources, or variable stars, have been shown to emit radiation throughout the electromagnetic spectrum, including the radio, optical, X-ray, and gamma-ray bands [17]. Various intrinsic and extrinsic physical mechanisms acting on these sources produce several types of emissions including object pulsations, eruptions, rotation, eclipses by companion stars, and cataclysmic effects, which have been observed and recorded for many celestial objects [18]. It has been shown that a subset of these variable sources, namely spinning neutron stars, or pulsars, have very regular, stable, periodic signals [11][12]. Remarkably, some pulsars have long term stabilities on the order of today's atomic clocks [8][13].

Astrophysical studies of the emitted signals from variable celestial sources have been utilized to characterize the parameters of these sources. For pulsars in particular, whose emissions can be accurately modeled due to their inherent periodicity, these studies have compared the observed pulse time of arrival (TOA) to the predicted pulse TOA using pulse timing models that are defined within the solar system barycentric inertial reference frame [11][12]. Careful analysis in defining these models, as well as the construction of precise detectors, is crucial to the accurate determination of a source's characteristic. Previous methods have created binned pulse profiles through extended observations of a specific source and folding the full observed signal with the expected pulse period of the source

[21]. These methods compute the observed pulse TOA by correlating an observed pulse profile with a high signal-to-noise profile template. Each observation must accurately time the pulse signal with respect to an inertial coordinate system and time, effectively removing the dynamic motion of the observation station and the relativistic effects on the electromagnetic signal within the solar system [1]. If the removal of motion and higher order contributions is done improperly, a smearing effect would be present within the observed pulse profile, and the uncertainty of the measured pulse TOA would increase.

Over the past decades, several works have considered exploiting the periodic nature of variable celestial sources for navigation of spacecraft within the solar system and beyond. Pulse TOA, or pulse phase, when measured by a moving spacecraft depends on the radial distance between the source and the spacecraft. Such measurements, therefore, convey information about the spacecraft's position. The feasibility of extracting this information and utilizing it for navigation purposes was investigated in [7][16][23], for sources that emit in the radio band. Similar concepts were examined in [5][16][19], for sources that emit in the X-ray band, primarily because smaller sized detectors can be utilized.

There are a number of X-ray sources with characteristics that are suitable for navigation purposes. Some are quite bright, emitting significant amounts of X-ray radiation, or flux, but many are faint, requiring larger sized detectors to collect a sufficient number of source photons over a given observation time interval. Other complications arise when sources exhibit unpredictable flares or output bursts, glitches in their rotation rates, and transient on-off durations. There is also an appreciable diffuse X-ray background radiation flux, which must be accounted for during the observation of any particular source [4]. Figure 1 provides an image of the Crab Nebula and its pulsar (PSR B0531+21) within the X-ray band. Sources such as the Crab Pulsar exhibit high-flux X-ray emissions with known periodicity and are, therefore, viable candidates for use in navigation.

This paper presents methods for determining the pulse TOA from the periodic signals emitted by variable celestial X-ray sources. Due to the inherent periodicity of these signals, the problem of pulse TOA estimation can be considered equivalently in the context of pulse phase estimation. The paper is organized in the following manner. First, a non-homogeneous Poisson random process is presented for modeling the arrival times of the X-ray photons. A maximum-likelihood phase estimator (MLE) is then presented for the case in which the observed signal frequency is constant and known over the observation interval. The Cramer-Rao theoretical performance bound is derived and evaluated for this parameter estimation problem. Next, a pulse phase tracking algorithm is presented for the case

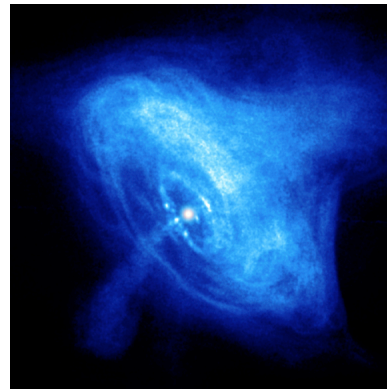


**Fig. 1** Crab Nebula and Pulsar (NASA/CXC/ASU/J. Hester et al.) [14].

in which the dynamical motion of the spacecraft over the observation interval results in considerable variation in the observed signal frequency. Tracking the phase of the observed pulse, as the vehicle progresses through its trajectory, provides a measure of the distance and rate of change of distance traveled during a given observation. Finally, numerical results are presented followed by a brief discussion of results and concluding remarks.

#### X-RAY SIGNAL MODEL AND SOURCE / DETECTOR CHARACTERISTICS

The arrival times of X-ray photons at the detector are modeled as a non-homogeneous Poisson process (NHPP) with a periodic or quasi-periodic rate function  $\lambda(t) \geq 0$ . In this representation, the number of photons arriving in a given time interval is a Poisson random variable. In other words, the probability of  $k$  photons arriving in the interval  $(a, b)$  is given by the expression [2][15]:

$$\Pr [k; (a, b)] = \frac{\left\{ \exp \left[ - \int_a^b \lambda(t) dt \right] \right\} \left[ \int_a^b \lambda(t) dt \right]^k}{k!} \quad (1)$$

$k = 0, 1, 2, \dots$  The rate function  $\lambda(t)$  represents the aggregate rate of all photons arriving at the detector from the source and background. The background photons arrive at a constant rate  $R_b$ . The source photons arrive at an average rate of  $R_s$  photons per second (ph/s) and consist of pulsed and non-pulsed photons, whose ratio is dictated by the pulsed fraction parameter, denoted  $\rho \leq 1$ . The pulsed fraction is defined as the ratio of the pulsed to total source photons. The non-pulsed source photons arrive at the constant rate of  $(1-\rho)R_s$ , and for all practical purposes behave the same as background photons. The pulsed source photons, however, exhibit a time-varying rate of arrival, which can be represented by the composition of two functions: the normalized pulse profile function,  $h(\phi)$ , and the pulsar observed phase at the detector,  $\phi_{det}(t)$ . The overall rate

function, therefore, consists of the following terms:

$$\lambda(t) = \underbrace{R_b + (1 - \rho)R_s}_{\equiv \beta} + \underbrace{\rho R_s}_{\equiv \alpha} h(\phi_{\text{det}}(t)) \quad (\text{ph/s}) \quad (2)$$

The parameters  $\alpha$  and  $\beta$  will be called the *effective source* and *background photon arrival rates*; they are the critical parameters with regards to performance. The pulse profile function  $h(\phi)$  is typically specified on the interval  $\phi \in (0, 1)$ ; however, in Eqn. (2), its definition is extended to any phase  $\phi \in (-\infty, +\infty)$  by letting  $h(m + \phi) = h(\phi)$  for all integers  $m$ , thus making  $h(\phi)$  a periodic function with its period equal to one cycle. The function  $h(\phi)$  is normalized and by definition satisfies the conditions:  $\min_{\phi \in (0,1)} h(\phi) = 0$ , and  $\int_0^1 h(\phi) d\phi = 1$ .

The observed phase at the detector can be expressed in terms of an initial phase and phase accumulated since beginning of the observation:

$$\phi_{\text{det}}(t) = \theta_0 + \int_{t_0}^t f(t') dt' \equiv \theta_0 + \theta(t) \quad (3)$$

where,

$$\begin{aligned} f(t) &\equiv \text{observed signal frequency} = f_s + f_d(t) \\ f_s &\equiv \text{source frequency (assumed constant)} \\ f_d(t) &\equiv \text{doppler frequency shift} = f_s v(t) / c \\ v(t) &\equiv \text{spacecraft range rate (radial speed)} \\ &\quad \text{in the direction towards the source} \end{aligned}$$

The source frequency,  $f_s$ , is assumed constant over the observation interval. This assumption, however, does not limit the scope of the ensuing analysis, since variations in the source frequency are often forecasted, and their effects can be removed through pre-processing of the photon TOA measurements. Also, the second and higher-order relativistic doppler effects have been ignored. The accumulated phase,  $\theta(t)$ , consists of the following two terms:

$$\theta(t) = f_s(t - t_0) + \underbrace{\int_{t_0}^t f_d(t') dt'}_{\equiv \theta_d(t)} \quad (4)$$

where  $\theta_d(t)$  will be referred to as the doppler phase. If range rate is a constant over the observation interval, or  $v(t) = v$ , then  $\theta(t)$  reduces to a strictly linear form:  $f_s(1 + v/c)(t - t_0)$ , and correspondingly, the Poisson rate function,  $\lambda(t)$ , is strictly periodic. On the other hand, if range rate is not a constant, then  $\theta_d(t)$  exhibits a non-linear dependence on time, resulting in a Poisson rate function that is quasi-periodic. These scenarios lead to the following two signal models.

**Constant-frequency model:** in which the observed signal frequency is a constant,  $f \equiv f_s(1 + v/c) \equiv 1/P$ , and phase evolves linearly at the detector,  $\phi_{\text{det}} = \theta_0 + f(t - t_0)$ . This model is considered when the detector is stationary or

is moving at a constant radial speed with respect to the pulsar, and the pulsar itself is undergoing negligible change in its period,  $P$ , over the observation interval. Substituting for  $\phi_{\text{det}}$  in Eqn. (2); the Poisson rate function can be written explicitly as a function of the initial phase and frequency parameters:

$$\lambda(t; \theta_0, f) = \beta + \alpha h(\theta_0 + f(t - t_0)) \quad (5)$$

The Poisson rate function is strictly periodic in this case, because  $h$  is strictly periodic, and its argument in Eqn. (5) is a linear (affine) function of time. The initial phase parameter,  $\theta_0$ , may also be regarded as a time shift parameter, since from Eqn. (5), it is evident that:  $\lambda(t; \theta_0, f) = \lambda(t + \tau; 0, f)$ , where  $\tau \equiv \theta_0/f = \theta_0 P$ . Hence, the problems of pulse time-of-arrival estimation ( $\tau$  modulo  $P$  seconds) and pulse phase estimation ( $\theta_0$  modulo one cycle) are the identical problems under this model.

**Time-varying frequency model:** is considered when the radial speed of the spacecraft in the direction of the source varies appreciably over the observation interval. In this case, the observed phase at the detector includes the phase variation due to doppler:  $\phi_{\text{det}} = \theta_0 + f(t - t_0) + \theta_d(t)$ , and the Poisson rate function is given by:

$$\lambda(t) = \beta + \alpha h(\theta_0 + f_s(t - t_0) + \theta_d(t)) \quad (6)$$

which is quasi-periodic due to  $\theta_d(t)$  causing the argument of  $h$  to deviate from the strictly linear form.

## MAXIMUM-LIKELIHOOD PULSE PHASE & FREQUENCY ESTIMATION

In this section, maximum-likelihood (ML) estimation of the pulse phase and frequency parameters is addressed under the constant frequency model. Let  $\{t_1, t_2, \dots, t_K\}$  denote the photon TOAs measured with a stable clock over the observation interval  $(t_0, t_0 + T_{\text{obs}})$ , where  $t_0 < t_k < t_0 + T_{\text{obs}}$  for  $1 \leq k \leq K$ . Our goal here is to estimate the model parameters  $\theta_0$  and  $f$  based on the observed realization of the non-homogeneous Poisson process (NHPP),  $\{t_k\}$ , whose time-varying expectation,  $\lambda(t; \theta_0, f)$ , has the known functional dependence on the estimation parameters given in Eqn. (5). The photon arrival rate parameters  $\alpha$  and  $\beta$ , and the normalized pulse profile function  $h(\phi)$ , are assumed to be known quantities.

The derivation of the ML estimator (MLE) presented below follows that of [2] with minor notational changes. We begin by noting the following consequences of adopting the NHPP model:

- The probability of zero photons arriving in the interval  $(a, b)$  is obtained by setting  $k = 0$  in Eqn. (1):

$$\Pr[0; (a, b)] = \exp\left[-\int_a^b \lambda(t) dt\right] \quad (7)$$

- The probability of one photon arriving in an infinitesimal time interval  $\xi$  of duration  $\Delta t$  centered around  $t$ , i.e. the interval  $\xi \equiv (t - \Delta t/2, t + \Delta t/2)$ , is given by evaluating Eqn. (1) for  $k = 1$ :

$$\Pr[1; (t - \Delta t/2, t + \Delta t/2)] = \lambda(t; \theta_0, f) \Delta t \quad (8)$$

as  $\Delta t \rightarrow 0$ .

- The probability of more than one photon arriving in  $\xi$  is zero for  $\Delta t \rightarrow 0$ .

- The number of photons arriving in any interval is independent of those in all other disjoint intervals.

The  $K$ -dimensional joint probability density function (pdf) of a given NHPP realization, denoted  $f(\{t_k\})$ , can be calculated by first considering an infinitesimal interval  $\xi_k$  of duration  $\Delta t_k$  centered around each  $t_k, k = 1, 2, \dots, K$ . The probability that one and only one photon arrives within each of these intervals and none outside of them is:

$$\begin{aligned} f(\{t_k\}) \Delta t_1 \Delta t_2 \dots \Delta t_K &= \Pr[0; (t_0, t_1 - \Delta t_1/2)] \\ &\times \Pr[1; (t_1 - \Delta t_1/2, t_1 + \Delta t_1/2)] \\ &\times \Pr[0; (t_1 + \Delta t_1/2, t_2 - \Delta t_2/2)] \\ &\vdots \\ &\times \Pr[1; (t_K - \Delta t_K/2, t_K + \Delta t_K/2)] \\ &\times \Pr[0; (t_K + \Delta t_K/2, t_0 + T_{\text{obs}})] \end{aligned} \quad (9)$$

Substituting Eqns. (7) and (8) into Eqn. (9), the following expression is obtained for the joint pdf by taking the limit  $\Delta t_k \rightarrow 0$  for all  $1 \leq k \leq K$ :

$$f(\{t_k\}) = \exp \left[ - \int_{t_0}^{t_0 + T_{\text{obs}}} \lambda(t; \theta_0, f) dt \right] \prod_{k=1}^K \lambda(t_k; \theta_0, f) \quad (10)$$

Recognizing the above joint pdf as the likelihood function, the ML estimator solves for the parameter values at which the likelihood function is maximized. Equivalently, logarithm of the likelihood function (LLF) can be maximized:

$$\text{LLF}(\tilde{\theta}_0, \tilde{f}) \equiv \sum_{k=1}^K \log[\lambda(t_k; \tilde{\theta}_0, \tilde{f})] - \int_{t_0}^{t_0 + T_{\text{obs}}} \lambda(t; \tilde{\theta}_0, \tilde{f}) dt \quad (11)$$

where  $\log$  is the natural logarithm, and  $\tilde{\theta}_0$  and  $\tilde{f}$  denote the test values at which the LLF is evaluated. When the observation interval spans many cycles of the signal at the hypothesized frequency (or  $fT_{\text{obs}} \gg 1$ ), as in most cases of interest, it can be shown that the integral in Eqn. (11) exhibits a minimal dependence on the search parameters  $\tilde{\theta}_0$  and  $\tilde{f}$ . Therefore, it can be dropped from the objective function for ease of computation in the optimization process. Substituting the constant frequency model of Eqn. (5) for  $\lambda(t; \theta_0, f)$  into Eqn. (11), the final optimization problem that the MLE

must solve is obtained: (12)

$$(\hat{\theta}_0, \hat{f}) = \arg \max_{\substack{\theta_0 \in \Theta, \\ f \in \Omega}} \underbrace{\sum_{k=1}^K \log[\beta + \alpha h(\tilde{\theta}_0 + \tilde{f}(t_k - t_0))]}_{\cong \text{LLF}(\tilde{\theta}_0, \tilde{f})}$$

The sets  $\Theta$  and  $\Omega$  denote the phase and frequency search spaces over which the LLF is to be maximized. The brute-force method of numerically solving the above optimization problem involves an iterative grid-search algorithm. It sets up an  $M_\Theta$ -by- $M_\Omega$  grid uniformly spanning the two-dimensional search space  $\Theta \times \Omega$  and proceeds to evaluate the LLF at each grid point. The grid point corresponding to the maximum computed LLF value is then selected as the phase and frequency estimates. The solution is refined by repeating this process over multiple iterations, where at each iteration a narrower phase and frequency interval, centered around the solution from the previous iteration, is searched. A-priori information about the parameters may be used to initially set the span of the phase and frequency search spaces before the first iteration.

When the signal frequency (including the doppler shift) is known to sufficient accuracy, the two-dimensional phase and frequency optimization of Eqn. (12) reduces to the following one-dimensional phase-only optimization:

$$\hat{\theta}_0 = \arg \max_{\theta_0 \in \Theta} \text{LLF}(\tilde{\theta}_0, f_{\text{ref}}) \quad (13)$$

by simply using the a-priori reference frequency (denoted  $f_{\text{ref}}$ ) in numerically evaluating the LLF function.

## THE CRAMER-RAO PERFORMANCE BOUND

The phase parameter estimation problem is now analyzed for the constant frequency model. Additionally, we assume the observed frequency,  $f$ , is known. In this case, the Poisson rate function takes on the form:  $\lambda(t; \theta_0) = \beta + \alpha h(\theta_0 + f(t - t_0))$ . Note that the following analysis may also be presented in terms of the pulse time-of-arrival, or pulse delay ( $\tau$ ) estimation.

Consider the problem of estimating the initial phase parameter,  $\theta_0$ , based on the measured photon arrival times. Partitioning the observation interval ( $t_0, t_0 + T_{\text{obs}}$ ) into  $N$  equal-length segments (or bins), the observation may alternatively be represented by the photon count sequence:  $X \equiv (X_0, X_1, \dots, X_{N-1})$ , where  $X_n$  is the number of photons counted in the  $n$ -th bin. Let  $\Delta t \equiv T_{\text{obs}}/N$  denote the bin size, and let it be arbitrarily small (or  $N$  arbitrarily large), so that the Poisson rate function  $\lambda(t; \theta_0)$  can be assumed slow-varying relative to  $\Delta t$ . In other words, assume that photons arrive at a constant rate:

$$\lambda_n(\theta_0) \equiv \lambda(\xi_n; \theta_0) \quad (14)$$

over the  $n$ -th bin, where the sequence  $\xi_n$  denotes the bin edges as depicted in Figure 2.

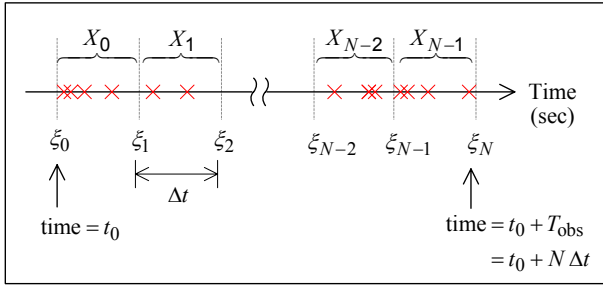


**Fig. 2** Photon binning and notation.

In estimation theory, the Cramer-Rao bound (CRB) places a lower bound on the variance of  $\hat{\theta}_0$ , where  $\hat{\theta}_0$  is any unbiased estimator of  $\theta_0$ :

$$\text{Var}(\hat{\theta}_0) \geq \text{CRB}(\theta_0) \equiv \frac{1}{-\text{E} \left[ \frac{\partial^2}{\partial \theta_0^2} \log \Pr(X; \theta_0) \right]} \quad (15)$$

and the expectation is taken with respect to  $\Pr(X; \theta_0)$  [9]. In evaluating (15), the probability mass function (pmf) for each of the Poisson random variables  $X_n$ ,  $n = 0, 1, \dots, N-1$ , can be written:

$$\Pr(X_n = x; \theta_0) = \frac{[\lambda_n(\theta_0) \Delta t]^x}{x!} \exp[-\lambda_n(\theta_0) \Delta t] \quad x = 0, 1, 2 \dots \quad (16)$$

The mean and variance of the Poisson random sequence,  $X_n$ , are given by:

$$\text{E}(X_n) = \text{Var}(X_n) = \lambda_n(\theta_0) \Delta t \quad (17)$$

Since  $X_n$  is an independent random sequence, the joint pmf for the sequence can be written as a product of pmf's of the individual random variables in the sequence, i.e.:

$$\begin{aligned} \Pr(X; \theta_0) &= \prod_{n=0}^{N-1} \Pr(X_n; \theta_0) \quad (18) \\ &= \prod_{n=0}^{N-1} \frac{[\lambda_n(\theta_0) \Delta t]^{X_n}}{X_n!} \exp[-\lambda_n(\theta_0) \Delta t] \end{aligned}$$

We proceed with the evaluation of the right-hand side expression in Eqn. (15):

$$\log \Pr(X; \theta_0) = \sum_{n=0}^{N-1} X_n \log [\lambda_n(\theta_0) \Delta t] - \log (X_n!) - \lambda_n(\theta_0) \Delta t \quad (19)$$

$$\begin{aligned} -\text{E} \left[ \frac{\partial^2}{\partial \theta_0^2} \log \Pr(X; \theta_0) \right] &= \sum_{n=0}^{N-1} \frac{\partial^2}{\partial \theta_0^2} (\lambda_n(\theta_0) \Delta t) \\ &\quad - \text{E}(X_n) \frac{\partial^2}{\partial \theta_0^2} (\log [\lambda_n(\theta_0) \Delta t]) \quad (20) \end{aligned}$$

dropping terms that do not depend on  $\theta_0$ .

Substituting (17) for  $\text{E}(X_n)$ :

$$\begin{aligned} \text{CRB}^{-1}(\theta_0) &= \sum_{n=0}^{N-1} \frac{\partial^2}{\partial \theta_0^2} (\lambda_n(\theta_0) \Delta t) - [\lambda_n(\theta_0) \Delta t] \\ &\quad \times \left\{ \frac{1}{\lambda_n(\theta_0) \Delta t} \frac{\partial^2}{\partial \theta_0^2} (\lambda_n(\theta_0) \Delta t) \right. \\ &\quad \left. - \left[ \frac{1}{\lambda_n(\theta_0) \Delta t} \frac{\partial}{\partial \theta_0} (\lambda_n(\theta_0) \Delta t) \right]^2 \right\} \\ &= \sum_{n=0}^{N-1} \frac{\left[ \frac{\partial}{\partial \theta_0} \lambda(\xi_n; \theta_0) \right]^2}{\lambda(\xi_n; \theta_0)} \Delta t \quad (21) \end{aligned}$$

Since  $\Delta t$  was taken to be an arbitrarily small interval, we may now take the limit  $\Delta t \rightarrow 0$ , or equivalently  $N \rightarrow \infty$ . In doing so, we replace the above summation with an integral:

$$\begin{aligned} \text{CRB}^{-1}(\theta_0) &= \int_{t_0}^{t_0 + T_{\text{obs}}} \frac{\left[ \frac{\partial}{\partial \theta_0} \lambda(t; \theta_0) \right]^2}{\lambda(t; \theta_0)} dt \\ &= \int_{t_0}^{t_0 + T_{\text{obs}}} \frac{\left[ \alpha \frac{\partial}{\partial \theta_0} h(\theta_0 + f(t - t_0)) \right]^2}{\beta + \alpha h(\theta_0 + f(t - t_0))} dt \\ &= \int_{\theta_0}^{\theta_0 + f T_{\text{obs}}} \frac{1}{f} \frac{\left[ \alpha \frac{\partial}{\partial \phi} h(\phi) \right]^2}{\beta + \alpha h(\phi)} d\phi \quad (22) \end{aligned}$$

Strictly speaking, the CRB of Eqn. (22) depends on the parameter  $\theta_0$ ; however, since the pulse profile function  $h(\phi)$  of the integrand is periodic, the dependence of the integral on  $\theta_0$  is either removed when  $f T_{\text{obs}}$  equals an integer number of cycles, or is insignificant when  $f T_{\text{obs}} \gg 1$  cycle. Assuming this to be the case, the CRB is obtained in its final form:

$$\text{Var}(\hat{\theta}_0) \geq \left[ T_{\text{obs}} \int_0^1 \frac{[\alpha h'(\phi)]^2}{\alpha h(\phi) + \beta} d\phi \right]^{-1} (\text{cycle}^2) \quad (23)$$

The CRB may also be stated in terms of the pulse TOA (or delay) estimation accuracy simply by dividing the above expression by  $f^2$ :

$$\text{Var}(\hat{\tau}) \geq \left[ f^2 T_{\text{obs}} \int_0^1 \frac{[\alpha h'(\phi)]^2}{\alpha h(\phi) + \beta} d\phi \right]^{-1} (\text{sec}^2) \quad (24)$$

## PULSE PHASE TRACKING ALGORITHM

Observers who are either stationary or move at a constant radial speed in the reference frame of the source will observe pulses that are strictly periodic over the observation interval. In these scenarios, the initial phase and frequency parameters,  $\theta_0$  and  $f$ , are entirely sufficient to characterize the instantaneous phase,  $\phi_{\text{det}}(t)$ , as it evolves over the observation interval. It is often the case, however, that ob-

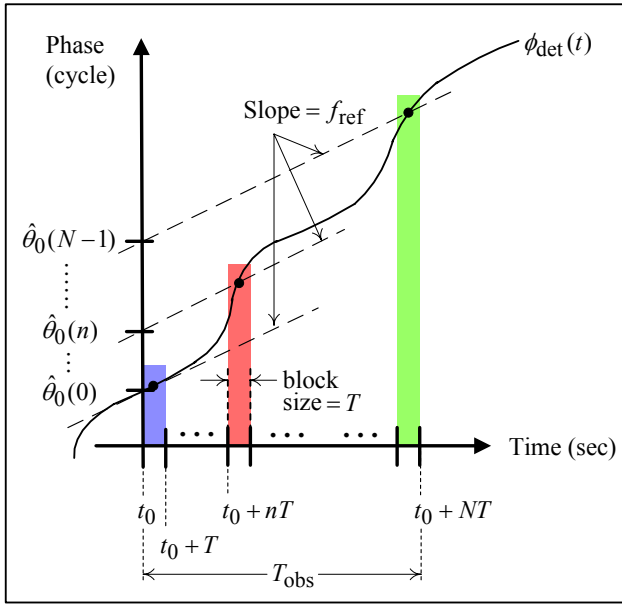


**Fig. 3** Diagram illustrating the pulse phase tracking concept for when the observed signal frequency is time-varying. Variations in the slope of  $\phi_{det}(t)$  are due to doppler and are exaggerated in the diagram for illustration purposes.

servations are made onboard a spacecraft that is traveling on a curved trajectory, and whose line-of-sight direction and radial speed toward the source varies appreciably over the length of the observation. In these cases, the observed frequency is not constant due to variations in the doppler shift, and the pulse epochs drift in an unpredictable manner throughout the observation as the spacecraft moves along its trajectory.

In this section, an algorithm is proposed for tracking the phase and frequency of an observed signal based on the time-varying frequency signal model. The main idea, illustrated in Figure 3, is to partition the observation interval into smaller subintervals, or *blocks*, such that the observed signal frequency is approximately constant over each block. Let  $T$  denote the duration of each block. Photons obtained over the  $n$ -th block are processed by the ML phase estimation algorithm to solve for the y-intercept,  $\hat{\theta}_0(n)$ , using Eqn. (13). If the reference frequency is set to:  $f_{ref} = f_s$ , then the y-intercepts in Figure 3 may be interpreted as:

$$\begin{aligned} \hat{\theta}_0(n) &= \text{Estimate of } \{ \phi_{det}(t) - f_s(t - t_0); t = t_0 + nT \} \\ &= \text{Estimate of } \{ \theta_0 + \theta_d(t); t = t_0 + nT \} \end{aligned}$$

Hence, the ML estimates track the phase quantity  $\theta_0 + \theta_d(t)$  over the observation interval by processing the photon TOA measurements one block at a time. One problem with this approach is that the sequence  $\hat{\theta}_0(n)$  may contain jumps due to phase wraparounds as well as a considerable amount of noise due to estimation errors. To address

the phase wraparound problem, we may consider searching the entire phase space  $\Theta = (0, 1)$  on processing the first block, but then for all subsequent blocks, set the search space to a suitably sized interval centered around the previous block's phase estimate. In this manner, the phase estimates are linked together, and may eventually wander outside of the initial  $(0, 1)$  search interval. The search intervals must be sufficiently large in order to guarantee that the signal phase stays within the search range of the MLE algorithm, given the signal dynamics and estimation errors involved.

In order to reduce the estimation errors or noise in the MLE output sequence, the estimates  $\hat{\theta}_0(n)$  may be post-processed either through a moving-average smoother, or a digital phase-locked loop (DPLL) filter [10][20]. In this paper, the MLE-DPLL cascade shown in Figure 4 is considered. Our implementation of the DPLL is second-order and follows closely that of [20].

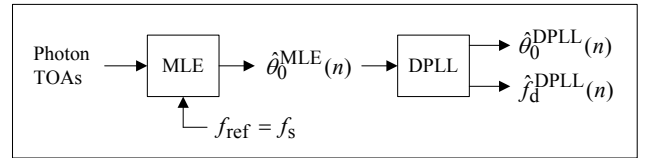


**Fig. 4** The MLE-DPLL cascade.

The operations of the DPLL is now described. First, an ideal phase detector calculates the difference between the input phase and the loop's phase estimate:

$$\tilde{\phi}(n) = \hat{\theta}_0^{MLE}(n) - \hat{\theta}_0^{DPLL}(n) \quad (25)$$

It is noted that phase additions and subtraction are carried out without wrapping (e.g.  $0.9 \text{ cycle} + 0.3 \text{ cycle} = 1.2 \text{ cycle}$ , not  $0.2 \text{ cycle}$ ). Next, the error feedback term  $\tilde{\phi}(n)$  is used to update the state of the loop filter [20]:

$$\hat{f}_d^{DPLL}(n+1)T = K_1 \tilde{\phi}(n) + K_2 \sum_{m=1}^n \tilde{\phi}(m) \quad (26)$$

Finally, the sequence,  $\hat{f}_d^{DPLL}(n+1)T$ , drives a numerically-controlled oscillator (NCO), dictating the phase amount by which the current NCO phase must be advanced over the next block in order to achieve the next phase estimate. At baseband, the NCO operation corresponds to the following phase accumulation process:

$$\hat{\theta}_0^{DPLL}(n+1) = \hat{\theta}_0^{DPLL}(n) + \hat{f}_d^{DPLL}(n+1)T \quad (27)$$

The phase state of the DPLL may be initialized according to:  $\hat{\theta}_0^{DPLL}(0) = \hat{\theta}_0^{MLE}(0)$ . The frequency state of the DPLL is initialized:  $\hat{f}_d^{DPLL}(0) = f_s \hat{v}(t_0)/c$ , when an estimate of range rate,  $\hat{v}(t_0)$ , is available; otherwise, it is set to zero.

## NUMERICAL RESULTS

In this section, the simulation setup shown in Figure 5 is used to analyze the performances of the MLE and the cascaded MLE-DPLL algorithms under the constant and time-varying frequency models, respectively.

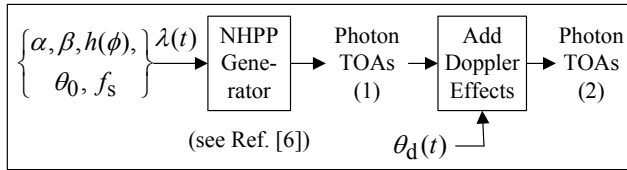


**Fig. 5** Non-homogeneous Poisson process (NHPP) generation and photon TOA simulation.

Three hypothetical scenarios were chosen to characterize performance over a range of operating conditions. The effective source and background arrival rates corresponding to these scenarios are listed in Table 1. It is noted, again, that  $\beta$  includes the non-pulsed source as well as background photon arrival rates.

Flux Scenario	$\alpha$ (ph/s)	$\beta$ (ph/s)
A	1,000	100
B	550	550
C	100	1,000

**Table 1** Simulated effective source and background photon flux scenarios.

The pulse profile shown in Figure 6 is representative of the Crab pulsar (PSR B0531+21) [22] and was used in simulating the photon TOAs. The initial phase parameter  $\theta_0$  was selected randomly on the interval  $(0, 1)$ , and the source frequency was set to:  $f_s = 29.8466$  Hz. Details of the NHPP generation are not discussed here, but the interested reader is referred to [6] (available online) for more information.

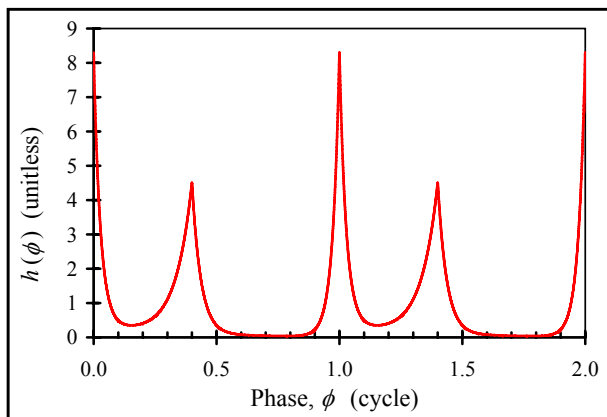


**Fig. 6** Normalized pulse profile function of the Crab pulsar [22] used in the simulation of photon arrival times.

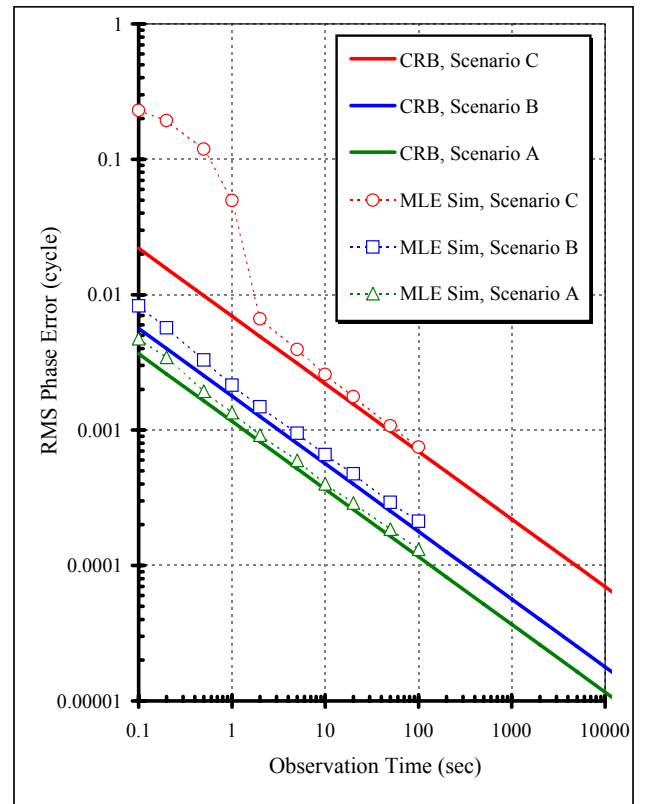


**Fig. 7** PSR B0531+21 (Crab pulsar) phase estimation accuracy under the three flux scenarios.

The performance of the MLE algorithm under the constant and known frequency model is simulated using the Monte-Carlo technique. The simulation results are plotted in Figure 7 and compared against the Cramer-Rao lower bound calculations. Photon TOAs labeled (1) in Figure 5 were processed by the MLE algorithm. The reference frequency,  $f_{\text{ref}}$ , was set equal to the source frequency,  $f_s$ . Each simulation point corresponds to 500 independent realizations of the NHPP process and subsequent calculation of the phase estimate,  $\hat{\theta}_0$ , according to Eqn. (13), searched on the interval  $\Theta = (0, 1)$ . The root-mean squared (RMS) phase error values were calculated via empirical averaging of the quantity,  $\min\{(\theta_0 - \hat{\theta}_0)^2, (\hat{\theta}_0 - \theta_0)^2\}$ . The minimum operator is necessary to ensure proper logging of the phase error values, since the error between 0.9 cycle and 0.1 cycle should be  $-0.2$  cycle, and not 0.8 cycle, when the phase variates are defined on the  $(0, 1)$  interval.

The CRB results are also plotted in Figure 7. They were calculated by numerically integrating the lower bound on variance, given in Eqn. (22). The CRB values shown in the plot are the square-root of the variances obtained from Eqn. (22). It is noted that for large observation times, the CRB predictions provide a tight lower-bound on performance; however, as the observation time is reduced, a *threshold* point is reached, at which the simulation results begin to deviate from the CRB (e.g., Scenario C, at  $T_{\text{obs}} \cong 2$  sec). At

this point, the number of source photons observed (on average) in each realization of the Poisson process reaches a critical limit. As the observation time is reduced below this threshold, realizations of the NHPP more frequently result in distorted log-likelihood surfaces whose global maxima do not lie in the vicinity of the true parameter value,  $\theta_0$ . This non-linear effect causes the estimate,  $\hat{\theta}_0$ , to become biased. In the limit, as the observation time is reduced even further beyond the threshold, the probability of receiving *any* source photon within the observation interval becomes small, and as a result, observations convey very little or no information about the observed signal phase or pulse TOA. In these cases, the phase estimate,  $\hat{\theta}_0$ , has a pdf that is almost uniformly distributed over the search space  $\Theta$  and is therefore clearly biased. Reference [24] provides good insight into the behavior of the MLE when operating in heavy noise and below threshold environments. It is presented in the context of delay estimation in the presence of additive white Gaussian noise.

The tracking problem is now analyzed, in which the photon TOAs labeled (2) in Figure 5 are processed through the MLE-DPLL cascaded algorithm. The doppler phase shown in Figure 8 is used to introduce motion effects into the simulated photon TOAs. It was obtained from actual GPS telemetry readouts of the Rossi X-ray Timing Explorer (RXTE) spacecraft while observing the Crab pulsar in orbit [3]. From the GPS position estimates, motion of the spacecraft projected in the LOS direction of the pulsar was determined. Range rate estimates were then transformed to doppler shift estimates through multiplication by the scale factor,  $f_s/c$ . A spline curve-fitting technique was used to obtain a smooth doppler frequency curve, which was numerically integrated to obtain the doppler phase profile shown in Figure 8. The initial phase,  $\theta_0 = 0.1$  cycle, was chosen arbitrarily.

For the DPLL tracking algorithm, the block duration was set to  $T = 1$  sec, and the DPLL was updated once per block.

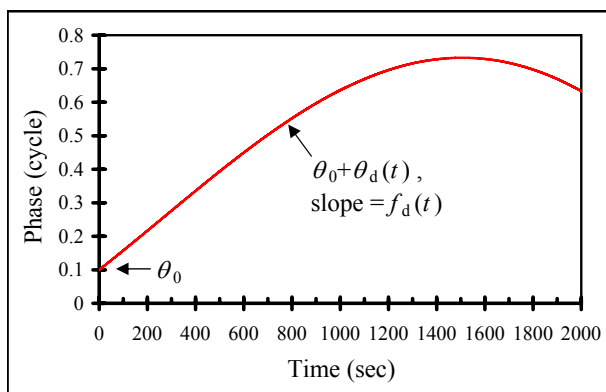


**Fig. 8** Doppler phase profile used in simulation, derived from an actual observation of the Crab pulsar as measured by the RXTE spacecraft.

The gain coefficients  $K_1$  and  $K_2$  were computed according to the design methodology outlined in [20]. Their values determine the traditional loop design parameters, namely: the loop noise bandwidth  $B_L$ , damping ratio  $\zeta$ , and natural frequency  $\omega_n$ . The following values for the loop noise bandwidth,  $B_L = 0.1, 0.05, 0.01$  Hz, and the damping ratio  $\zeta = 0.707$  (standard underdamped response), were considered. These settings resulted in the gain coefficients listed below:

Loop Bandwidth $B_L$ (Hz)	$K_1$	$K_2$
0.10	0.2179	0.02670
0.05	0.1199	0.007658
0.01	0.02609	0.0003448

**Table 2** Loop filter constants (from Table VI of [20]). Fixed design parameters were:  $\zeta = 0.707$  and  $T = 1$  sec.

Figures 9-10 show the phase and frequency estimates of the DPLL as it acquires and tracks its input signal. Note that phase *error* values (and not the phase varies themselves) are plotted in order to better show the transient phase response of the loop. The phase and frequency states of the DPLL were initialized to zero at the start. This corresponded to an initial phase error of  $-0.1$  cycle, and an initial frequency error of  $-0.5666$  mHz.

In Figure 9, the presence of a bias is observed in the DPLL phase estimates. This is due to the fact that the signal dynamics exhibits a nonzero acceleration. In other words, the second derivative of  $\theta_d(t)$  in Figure 8 is nonzero, but the signal is being tracked using a second-order DPLL. This suggests that a third-order DPLL is required if one wishes to remove this bias. Our objective, however, may be to obtain estimates of the doppler frequency, in which case the DPLL frequency estimates shown in Figure 10 are adequate, as they appear to be unbiased. A smaller loop noise bandwidth results in smaller frequency estimation errors, but requires a longer settling time to overcome the initial frequency uncertainty. The phase bias and RMS frequency errors corresponding to Figures 9 and 10 are provided numerically in Table 3. They were calculated by discarding the first 500 sec of the data to allow the initial settling time to elapse.

Loop Bandwidth $B_L$ (Hz)	Phase Bias ( $\times 10^{-3}$ cycle)	RMS Frequency Error ( $\times 10^{-3}$ Hz)
0.10	0.686	0.331
0.05	0.700	0.177
0.01	2.393	0.034

**Table 3** Second-order DPLL, phase bias and RMS frequency error performances corresponding to tracking of the signal in Figure 8, under flux scenario A.



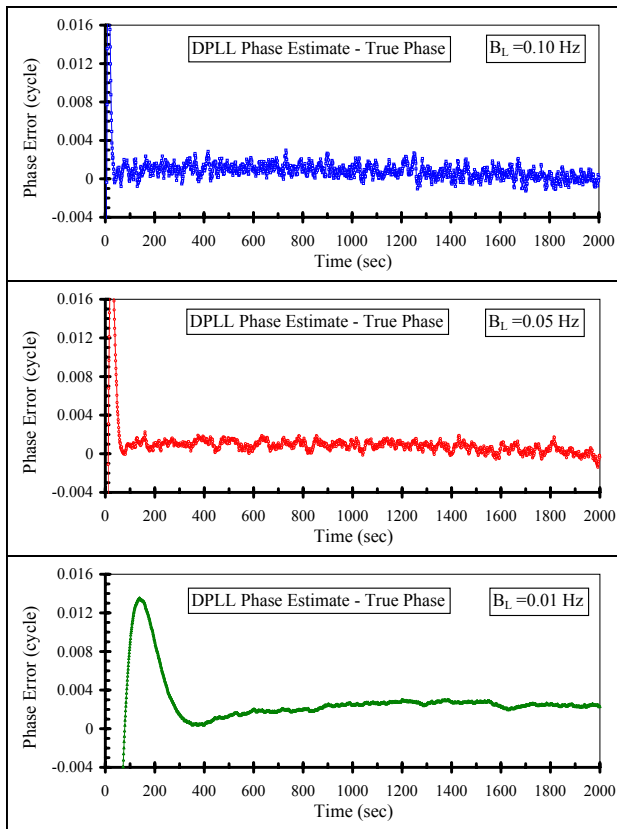


**Fig. 9** DPLL simulated doppler phase tracking (Crab pulsar, flux scenario A,  $T = 1$  sec).

Finally, it is noted that the RMS error (RMSE) results shown in Figure 7 may be transformed from phase accuracy into either pulse TOA accuracy or range accuracy, using the relationships:

$$\begin{aligned} \text{RMSE}(\text{ pulse phase } ) &= \text{RMSE}(\text{ pulse TOA } ) \times f_s \\ &= \text{RMSE}(\text{ range } ) \times \frac{f_s}{c} \end{aligned}$$

Similarly, the doppler frequency estimates in Figure 10 can be transformed into pulse TOA rate, or range rate estimates.

## CONCLUSION

Accurate phase estimation and tracking of signal pulses is an important aspect of utilizing these signals for practical applications such as spacecraft navigation. In this paper, a maximum-likelihood phase estimator was presented for the case in which the observed signal frequency is constant and known over the observation interval. The performance of this algorithm was analyzed through simulation of photon TOAs under various signal and noise flux conditions. The performance of the ML estimator was shown to be optimal as it attained the Cramer-Rao performance bound once the source observation exceeded a certain threshold in duration. Higher source flux scenarios resulted in the ML es-

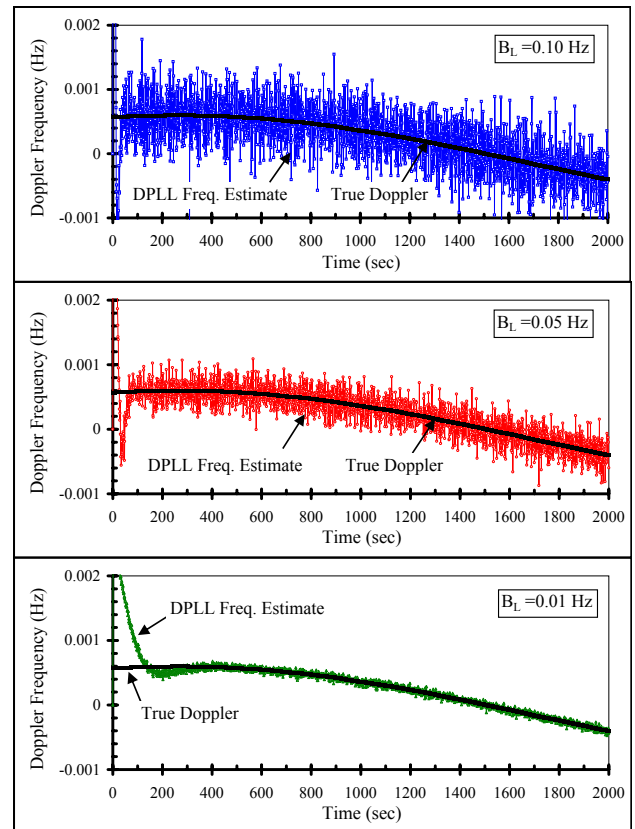


**Fig. 10** DPLL simulated doppler frequency tracking (Crab pulsar, flux scenario A,  $T = 1$  sec).

imator achieving the optimal performance at shorter observation times. This paper also presented a pulse phase tracking algorithm for the case in which the dynamical motion of the spacecraft causes the observed signal frequency to vary considerably over the observation interval. A cascaded MLE-DPLL algorithm was proposed, and the frequency estimates of the DPLL were shown to provide unbiased estimates of the doppler frequency.

## ACKNOWLEDGMENTS

The authors wish to thank Daniel Jablonski, John Golden, Kenneth Nelson, and Bob Henderson of JHU/APL for their contributions on this research. They would also like to thank Darryll Pines, Program Manager of the DARPA X-ray Navigation and Autonomous Position Verification (XNAV) program, for his encouragement on pursuing this topic, as well as all the XNAV team members for their helpful discussion on this topic. This research has made use of data obtained from the High Energy Astrophysics Science Archive Research Center (HEASARC), provided by NASA's Goddard Space Flight Center.

Distribution Statement: Approved for Public Release, Distribution Unlimited.

## REFERENCES

- [1] Backer, D. C., and Hellings, R. W., "Pulsar Timing and General Relativity," *Annual Review of Astronomy and Astrophysics*, Vol. 24, 1986, pp. 537-575.
- [2] Bar-David, I., "Communication under the Poisson Regime," *IEEE Transactions on Information Theory*, Vol. 15, No. 1, January 1969, pp. 31-37.
- [3] Bradt, H. V., Rothschild, R. E., and Swank, J. H., "X-ray Timing Explorer Mission," *Astronomy and Astrophysics Supplement Series*, Vol. 97, 1993, pp. 355-360.
- [4] Charles, P. A., and Seward, F. D., *Exploring the X-ray Universe*, Cambridge University Press, Cambridge UK, 1995.
- [5] Chester, T. J., and Butman, S. A., "Navigation Using X-ray Pulsars," *NASA Technical Reports N81-27129*, 1981, pp. 22-25.
- [6] Devroye, L., *Non-Uniform Random Variate Generation*, Chapter VI, Springer-Verlag, 1986, [online book], URL: <http://cg.scs.carleton.ca/~luc/rnbookindex.html> [cited April 1, 2007].
- [7] Downs, G. S., "Interplanetary Navigation Using Pulsating Radio Sources," *NASA Technical Reports N74-34150*, 1974, pp. 1-12.
- [8] Kaspi, V. M., Taylor, J. H., and Ryba, M. F., "High-Precision Timing of Millisecond Pulsars. III: Long-Term Monitoring of PSRs B1855+09 and B1937+21," *Astrophysical Journal*, Vol. 428, 1994, pp. 713-728.
- [9] Kay, S. M., *Fundamentals of Statistical Signal Processing: Estimation Theory*, Chapter 3, Prentice Hall, New Jersey, 1993.
- [10] Lindsey, W. C., and Chie, C. M., "A Survey of Digital Phase-Locked Loops," *IEEE Proceedings*, Vol. 69, April 1981, pp. 410-431.
- [11] Lyne, A. G., and Graham-Smith, F., *Pulsar Astronomy*, Cambridge University Press, Cambridge UK, 1998.
- [12] Manchester, R. N., and Taylor, J. H., *Pulsars*, W.H. Freeman and Company, San Francisco CA, 1977.
- [13] Matsakis, D. N., Taylor, J. H., and Eubanks, T. M., "A Statistic for Describing Pulsar and Clock Stabilities," *Astronomy and Astrophysics*, Vol. 326, 1997, pp. 924-928.
- [14] NASA/CXC/SAO, "Time Lapse Movies of Crab Nebula," [online], URL: <http://chandra.harvard.edu/photo/2002/0052/movies.html> [cited 1 June 2003].
- [15] Papoulis, A., *Probability, Random Variables, and Stochastic Processes*, Third Edition, McGraw-Hill, New York, 1991.
- [16] Sala, J., Urruela, A., Villares, X., Estalella, R., and Paredes, J. M., "Feasibility Study for a Spacecraft Navigation System relying on Pulsar Timing Information," European Space Agency Advanced Concepts Team ARIADNA Study 03/4202, 23 June 2004.
- [17] Samus, N. N., and Durlevich, O. V., "General Catalogue of Variable Stars," *VizieR Online Data Catalog*, Vol. 2250, 2004.
- [18] Samus, N. N., and Durlevich, O. V., "General Catalogue of Variable Stars (GCVS) Variability Types and Distribution Statistics of Designated Variable Stars According to their Types of Variability," [online database], URL: <http://www.sai.msu.su/groups/cluster/gcvs/gcvs/iii/vartype.txt> [cited 7 March 2005].
- [19] Sheikh, S. I., Pines, D. J., Wood, K. S., Ray, P. S., Lovellette, M. N., and Wolff, M. T., "Spacecraft Navigation Using X-ray Pulsars," *Journal of Guidance, Control, and Dynamics*, Vol. 29, No. 1, 2006.
- [20] Stephens, S. A., and Thomas, J. B., "Controlled-Root Formulation for Digital Phase-Locked Loops," *IEEE Transactions on Aerospace and Electronic Systems*, Vol. 31, No. 1, January 1995, pp. 78-95.
- [21] Taylor, J. H., "Pulsar Timing and Relativistic Gravity," *Philosophical Transactions of the Royal Society of London*, Vol. 341, 1992, pp. 117-134.
- [22] Tennant A. F., et al., "Discovery of X-Ray Emission From the CRAB Pulsar at Pulse Minimum", *The Astrophysical Journal*, 554:L173-L176, 2001 June 20.
- [23] Wallace, K., "Radio Stars, What They Are and The Prospects for their Use in Navigational Systems," *Journal of Navigation*, Vol. 41, No. 3, 1988, pp. 358-374.
- [24] Weaver, R.D., "No information? Delay Estimation Below the Threshold SNR," Thirty-Ninth Asilomar Conference on Signals, Systems and Computers, October 28 - November 1, 2005, pp. 1104-1108.